Materials Science in Semiconductor Processing 203 (2026) 110253

Contents lists available at ScienceDirect

Materials Science in Semiconductor Processing

journal homepage: www.elsevier.com/locate/mssp

# Conductance quantization in memristive devices with electrodeposited Prussian blue-based dielectrics

A. Cantudo [a], L.B. Avila [b], M.A. Villena [a], F. Jiménez-Molinos [a], C. Ducarme [b], A. Lopes Temporao [b], A. Moureaux [b], F. Abreu Araujo [b], C.K. Müller [c], J.B. Roldán [a,d,*]

[a] Departamento de Electrónica y Tecnología de Computadores, Universidad de Granada, Facultad de Ciencias, Avd. Fuentenueva s/n, 18071, Granada, Spain
[b] Institute of Condensed Matter and Nanosciences (ICMN), Université Catholique de Louvain (UCLouvain), Louvain-la-Neuve, B-1348, Belgium
[c] Faculty of Physical Engineering/Computer Sciences, University of Applied Sciences Zwickau, 08056, Zwickau, Germany
[d] Institute "Carlos I" for Theoretical and Computational Physics, University of Granada, 18071, Granada, Spain

ARTICLE INFO

*Keywords:*
Memristors
Prussian blue
Resistive memory
Conductance quantization
Current modeling

ABSTRACT

Identifying new, scalable materials for memristive devices is critical to advance next-generation memory and neuromorphic technologies. In this context, electrodeposited Prussian Blue (PB), a mixed-valence iron hexacyanoferrate compound, is emerging as a highly promising candidate due to its low-cost synthesis, CMOS compatibility, and rich redox chemistry. Here, we report both experimental evidence and theoretical modeling of conductance quantization in memristive devices employing PB as the active dielectric layer. PB thin films were synthesized via electrodeposition and integrated into a conventional metal–insulator–metal (*MIM*) structure (Ag/PB/Au), which exhibits robust and reproducible resistive switching behavior. Notably, we observe quantized conductance steps at integer and half-integer multiples of the quantum of conductance ($G_0 = 2e2/h$), indicative of atomic-scale filament formation and ballistic electron transport. To interpret these findings, we use a quantum transport model based on the finite-bias Landauer formalism, incorporating a series resistance and a non-ideality parameter ($\alpha$), which successfully reproduces the experimental $I-V$ characteristics. An algorithm is also introduced to extract the model parameters directly from measured data. The emergence of quantized states is attributed to the properties of PB due to its open-framework structure, mixed $Fe2^{+}/Fe3^{+}$ valence, and reversible ionic mobility, which allow the formation of atomic conduction channels. These results highlight the potential of PB-based memristors for multilevel memory storage and neuromorphic computing, while offering a scalable, CMOS-compatible, and sustainable materials platform.

## 1. Introduction

Memristive devices are linked to outstanding industrial products that are currently being commercialized and show great potential for the future IC market [1–3]. Some of the more relevant applications are connected to non-volatile memory circuits, where top players, such as TSMC and INTEL, are incorporating memristive devices in their technology [4–6]. Neuromorphic engineering [7] is growing at present by leaps and bounds due to the role played by memristive devices; in this context, the academy and industry are working to implement hardware neural networks to accelerate AI training and inference processes [8–23]. Cryptographic systems can also benefit from the use of memristive devices due to their inherent random behavior that facilitates the fabrication of entropy sources [1,24,25], which are essential for building true random number generators [26] and physical unclonable functions [27].

Many memristive devices [28,29] show resistive switching (RS) that permits them to drastically change their internal conductance. Multilevel operation in memristive devices is feasible and enables mimicking biological synapses within the neuromorphic computing approach. In particular, resistive memories, a subset of memristive devices [30], switch their internal resistance through processes linked to ionic transport [31]; in this respect, their operation is close to synaptic connections in mammals' neural tissue [11,17,23,32].

Digital operation of resistive memories (also known as Resistive Random Access Memories, RRAM) enables non-volatile memory

* Corresponding author. Departamento de Electrónica y Tecnología de Computadores, Universidad de Granada, Facultad de Ciencias, Avd. Fuentenueva s/n, 18071, Granada, Spain.
*E-mail address:* jroldan@ugr.es (J.B. Roldán).

https://doi.org/10.1016/j.mssp.2025.110253
Received 17 September 2025; Received in revised form 30 October 2025; Accepted 6 November 2025
Available online 12 November 2025

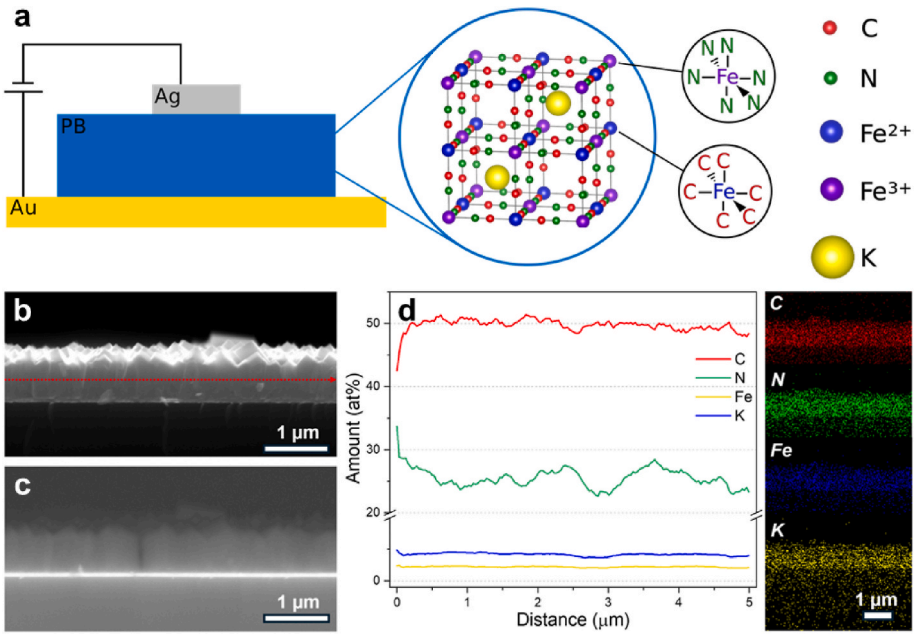


**Fig. 1.** **a** Schematic of the Ag/PB/Au layer sequence, configuration of the final device for electrical measurements, and next to it the structure of the $KFe[Fe(CN)_6$ crystal model as well as the respective chemical bonds that the $Fe^{2+}/Fe^{3}$ pair has. **b** SEM and EDX-analysis of PB film performed at 15 keV: SEM cross-section image (obtained with secondary electrons) of the investigated sample region used for line-scan analysis, **c** corresponding SEM cross-section image obtained by detection of backscattered electrons. **d** Elemental composition obtained by line-scan analysis along the marked line in **(b)** and corresponding elemental maps.

applications; however, the analog perspective, which can be materialized in the context of multilevel switching, is also essential. In this respect, different conductance levels can be achieved by means of algorithms utilizing low voltage pulses [12,33] or through switching under different compliance currents [34,35]. A third way to articulate multilevel operation is linked to conductance quantization that comes up in certain types of RRAM [36]. Conductance quantization leads to levels separated by multiples of the quantum unit of conductance, $G_0 = 2e_2/h = 77.5\ \mu S$ (e is the electron charge and h is Planck's constant). This effect shows up under the ballistic transport regime that occurs if the electron elastic mean free path (a quantity that accounts for the average distance between elastic collisions) is higher than the system size. In the case of RRAM with filamentary conduction, this means a nanometric constriction in a conductive filament (CF) [37,38]. Under this regime, the electron momentum can be assumed to be constant, only changed by scattering in the reservoirs on both sides of the nanometric constriction. For Ag and Cu, typical metals employed for electrode fabrication in resistive memories, the elastic mean free paths are 53.3 nm and 39.9 nm, respectively [39]. Therefore, when considering CFs made of regions with a high concentration of Ag or Cu atoms, with constrictions a few nanometers wide, it is clear that the transport regime is far from being diffusive. Conductance quantization was first reported in 1988 in a two-dimensional electron gas formed in a GaAs/AlGaAs heterostructure [40]; later, this effect was also observed in atomic quantum contacts [41], nanotubes [42], and mechanically controllable break junctions [43]. It has also been reported in resistive memories at room temperature for a wide variety of dielectric materials [36,44–46]. Although the applications of conductance quantization are rather unexplored, as stated in Ref. [36], several authors have proposed that conductance quantization engineering in resistive memories can be employed to address multilevel operation in the memory context, and also to deal with quantum information processing and neuromorphic systems [45,47].

In line with these results, we present here the characterization and modeling of conductance quantization in RRAM devices employing dielectrics based on Prussian Blue (PB). PB thin films are easily deposited by electrodeposition, a highly versatile, low-cost, solution-based technique that allows precise control over film thickness, morphology, and uniformity directly onto conductive substrates from aqueous solutions.

Previous studies have demonstrated that PB is a promising material for memristive device applications, owing to its mixed-valence chemistry, robust redox reversibility, and open-framework structure [48–52]. PB is a mixed-valence iron(III/II) hexacyanoferrate compound with a distinctive face-centered cubic structure. In this framework, $Fe3^{+}$ ions are coordinated through nitrogen atoms, while $Fe^{2+}$ ions are coordinated through carbon atoms, forming a repeating $Fe^{3+} - N \equiv C - Fe^{2+} - C \equiv N - Fe^{3+}$ chain throughout the lattice. Its characteristic deep blue color arises from the high degree of structural order and is closely associated with intervalence charge transfer between iron centers [53].

Moreover, the substitution of iron with other transition metals generates a wide family of Prussian Blue analogues (PBAs), significantly expanding the design space for tailoring their electronic, ionic, and catalytic properties [54]. This tunability is enabled by their open-framework structure, rich redox chemistry, and composition-dependent characteristics, which collectively facilitate efficient ionic transport [51,55]. Furthermore, PBAs are composed of earth-abundant elements (e.g., Fe, C, N, K), making them cost-effective, environmentally benign, and synthetically accessible. This unique combination of tunable functionality and practical manufacturability makes them exceptionally promising for scalable device fabrication and seamless integration into next-generation microelectronic architectures [56].

Section 2 is devoted to fabrication details and the measurement setup; in Section 3, we deal with the results and modeling. Finally, some conclusions are drawn in Section 4.

## 2. Device fabrication and measurement setup

The dielectric layer, composed of a PB film, was deposited at room temperature by means of an electrochemical process conducted in potentiostatic mode using an electrochemical workstation (Ivium CompactStat, Eindhoven, Netherlands). The electrodeposition was carried out in a conventional three-electrode electrochemical cell, with all

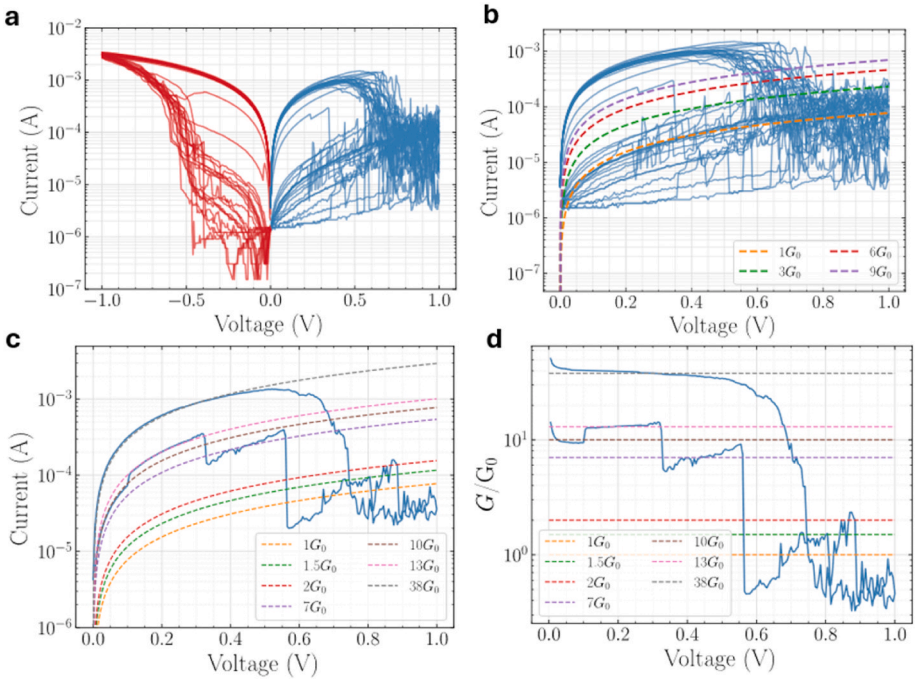


**Fig. 2.** **a** Experimental current versus voltage for Ag/PB/Au devices, for set and reset processes. **b** Experimental reset cycles (solid blue lines) and different current curves (dashed lines) corresponding to multiples of the quantum unit of conductance, $G_0$. **c** Experimental current versus voltage (solid blue line), corresponding to cycle 80, where quantization is observed in some parts of the curve. Theoretical curves corresponding to $G_0$ multiples and half-integers are shown for comparison in dashed lines. **d** Experimental normalized conductance corresponding to cycle 80 (solid blue lines), where the conductance quantization is depicted compared with $G_0$ multiples and half-integer multiples. The latter ones are justified theoretically in Ref. [45], accounting for tunneling effects from both electron reservoirs to the atomic-size constraint separately. (For interpretation of the references to color in this figure legend, the reader is referred to the Web version of this article.)

electrodes connected to a potentiostat. The working electrode (WE) consisted of an *Au*/*Cr*/*Si* substrate, fabricated by evaporating a 5 *nm* chromium adhesion layer followed by a 50 *nm* gold layer onto a (100)-oriented silicon wafer (1 *cm* ×1 *cm*) under a base pressure of $10^{-5}$ *Pa*. During sample preparation, the PB film was electrochemically deposited onto a circular area of 0.5 $cm^2$ (the fabrication electrode), defined by an adhesive tape mask, to confine the film growth region. Later, the final electrode area was reduced by a factor of 100. A platinum foil served as the counter electrode (CE), and a saturated calomel electrode (SCE) was used as the reference electrode (RE). The electrolyte solution contained 1.0 *M KCl*, 5.0 *mM HCl*, 0.5 *mM* $FeCl_3$, and 0.5 *mM* $K_3Fe(CN)_6$ (ACS, >99 % Sigma Aldrich, Darmstadt, Germany dissolved in 100 *mL* of deionized water and adjusted to *pH* 2). A constant potential of 0.3 *V* at SCE was applied at 25°*C*, and the electrodeposition process was precisely controlled by limiting the total deposited charge to 30*mC*, resulting in an estimated PB film thickness of approximately 500*nm*, as previously discussed in detail in Ref. [57], which also provides further details on the three-electrode electrochemical cell configuration. Notably, our samples require no post-deposition thermal or chemical treatments, simplifying the fabrication process and reducing overall processing complexity. In the Supplementary Information, we deal with physical characterization issue of our samples. In particular, X-ray diffraction measurements (Fig. S1) are shown for PB films, the cubic crystalline structure is in good agreement with results previously reported; Raman spectroscopy was also employed to analyze its chemical composition (Fig. S2). The Raman spectrum clearly confirms the deposition of PB without other impurities.

The final device structure comprised a silver top electrode (formed by drop-casting onto the PB surface, with a thickness in the micrometer range), the PB dielectric layer, and a gold bottom electrode, shown in Fig. 1a. The $I-V$ characterization was performed at room temperature using a Keithley 2400 programmable electrometer in a two-point probe configuration, applying a DC voltage sweep from $-1$ *V* to $+1$ *V* at a ramp rate of 5 *mV*/*s*. One hundred consecutive cycles were measured, revealing consistent resistive switching behavior. The transition from low-resistance state (LRS) to high-resistance state (HRS) occurred at positive voltages, while the reset (HRS to LRS) transition was observed at negative voltages. The observed cycle-to-cycle variability [58] was within acceptable limits and discussed in detail in Ref. [57]. The physical mechanisms behind RS in this technology stand upon $K^+$ migration, the EDX analysis confirms the presence of potassium near the dielectric surface. Under an applied electric field, the $K^+$ ions can migrate through the framework, contributing to the conductive filaments formation and rupture. These mechanisms are in line with the findings reported in Ref. [50].

Fig. 1b shows the morphology and elemental composition of PB, analyzed using field emission scanning electron microscopy (FEG-SEM, TESCAN CLARA, Brünn, Czech Republic) equipped with an energy-dispersive X-ray (EDX) detector (Ultim Max 65 SDD, Oxford Instruments, Wiesbaden, Germany) operated at 15 keV. Additionally, the chemical composition of the samples was examined by Raman spectroscopy (WITec RISE, Ulm, Germany), performed within the electron microscope, as presented in Fig. 1d. Raman measurements were conducted using a 532 nm laser at a power of 0.5 mW.

## 3. Results, discussion, and modeling

### 3.1. Experimental results

The devices described in the previous section were measured, and some of the I-V curves of a long RS series are shown in Fig. 2a, where bipolar RS is observed. From this figure, we can see the large difference in current between the HRS and LRS, which makes these devices suitable for non-volatile memory applications. It is important to highlight that the current levels of all successive steps of the measured I-V curves (mostly in the HRS after the reset events, Fig. 2b) have values the order of a few multiples of the quantum unit of conductance, $G_0$. A more detailed view of several current curves allows to realize that some parts

**Table 1**
Different memristor structures showing conductance quantization effects. In the column linked to the conductive filament type, Vo stands for filaments made of oxygen vacancies.

| Reference | Stack structure | Conductive filament type | RS polarity |
|---|---|---|---|
| [59] | $Ag_2S$ or $Cu_2S$ | Ag | Bipolar |
| [60] | Ag/$Ag_2S$/W | Ag | Bipolar |
| [61] | Ag/AgI/Pt | Ag | Bipolar |
| [62] | Ag/$Ta_2O_5$/Pt | Ag | Bipolar |
| [63] | Ag/$Ag_2S$/Pt | Ag | Bipolar |
| [64] | Ag/$GeS_2$/W | Ag | Bipolar |
| [66] | Nb/$ZnO_x$/Pt | Nb or Vo | Bipolar |
| [65] | ITO/$ZnO_x$/ITO | Vo | Unipolar |
| [67] | W/$CeO_x$/$SiO_2$/$NiSi_2$ | Vo | Bipolar |
| [68] | Pt/$HfO_2$/Pt | Vo | Unipolar |
| [69] | Ag/$P_3$HT:PCBM/ITO | Ag | Bipolar |
| [70] | Ag/a-$La_{1-x}Sr_xMnO_3$/Pt | Ag | Bipolar |
| [71] | Pt/$HfO_2$/Pt | Vo | Unipolar |
| [72] | Ti (Ta, W)/$Ta_2O_5$/Pt | Vo | Bipolar |
| [45] | n-Si/$SiO_x$/p-Si | Vo | Uni/Bipolar |
| [73] | Ti/$HfO_2$/TiN | Vo | Bipolar |
| [74] | Ti/$TiO_2$/$SrTiO_3$ | Vo | Bipolar |
| [75] | Ag/$SiO_2$/Au (W) | Ag | Bipolar |
| [76] | Ag/$SiO_2$/Pt | Ag | Bipolar |
| [77] | Cu/$HfO_x$/Pt | Cu | Bipolar |
| [78] | Cu/$TiO_2$/Pt | Cu | Bipolar |
| [79] | Ag/AlST/Ta | Ag | Bipolar |
| [80] | Ti/$TiO_2$/Nb-$SrTiO_3$ | Vo and Ti | – |
| [81] | Pt/$Nb_2O_5$/Al | Pt and Vo | Unipolar |
| [82] | Pt/$HfO_2$/Pt | Vo | Bipolar |
| [83] | Pt/$Gd_2O_3$/ITO | Vo | Bipolar |
| [84] | TiN/Ti/HfOx/TiN | Vo | Bipolar |
| [85] | Ag/hBN/Ag | Ag | Bipolar |
| [86] | Pt/NiO/Pt | Vo | – |
| [87] | Cu/PPX/ITO | Cu | Bipolar |
| [44] | Au/Ti/h-BN/Au/Ti | Au | Bipolar |
| [88] | Pt/$Mn_3O_4$/Pt | Pt | Bipolar |

of the curve can be exactly reproduced by curves corresponding to $G_0$ multiples (Fig. 2c). The conductance plot of the same experimental measurements (Fig. 2d) also shows a picture of quantization effects that, as already highlighted above, have also been reported in other RRAM technologies at room temperature [36,44–46]. In order to describe this latter issue in a more organized manner, we have included Table 1, where different devices that showed conductance quantization are listed.

Similarly, the conductance quantization effects can be seen in set curves, as shown in Fig. 3 for different cycles.

### 3.2. Current modeling

RRAM current modeling accounting for conductance quantization has been addressed from different perspectives in the last few years [36–38,44]. Considering a set (or a bundle) of atomic-size paths (constrictions) in parallel (see Fig. 4a), we employ the finite-bias Landauer's approach. Neglecting inelastic interactions (which is reasonable in this context), the conductance is linked to the transmission probability in the constrictions. Taking into account the electron influx from each electrode through the constrictions and considering an equal voltage drop at the constriction sides, the number of conduction modes can be obtained [45]. Assuming a low constriction energy barrier that does not hinder the charge flux (i.e., the transmission probability is supposed to be 1), the device current is described as follows [45],

$$I = \frac{1}{2}(n_L + n_R)G_0 V \tag{1}$$

where $n_R$ and $n_L$ stand for the number of occupied subbands accessed from the constriction right and left sides (from the electron reservoirs, viewing it from another perspective [36,45,89]). The sum ($n_R + n_L$) can be an even or odd number. To further improve the model, the inclusion of a resistance in series [90] with the bundle of atomic-size paths that produce the conductance quantization is needed [44,91]. The series resistance ($R_{series}$) accounts for the ohmic transport linked to conductive filament remnants and the contribution of metal pads (see Fig. 4a). Taking into account this resistance in Eq. (1), the current is given by Expression 2 [91],

$$I \approx \frac{n\,G_0}{1 + n\,G_0 R_{series}} V \tag{2}$$

where n is the number of modes (or subbands) available for conduction [44,91]. For the sake of simplicity, we will use n instead of $1/2\cdot(n_R +$

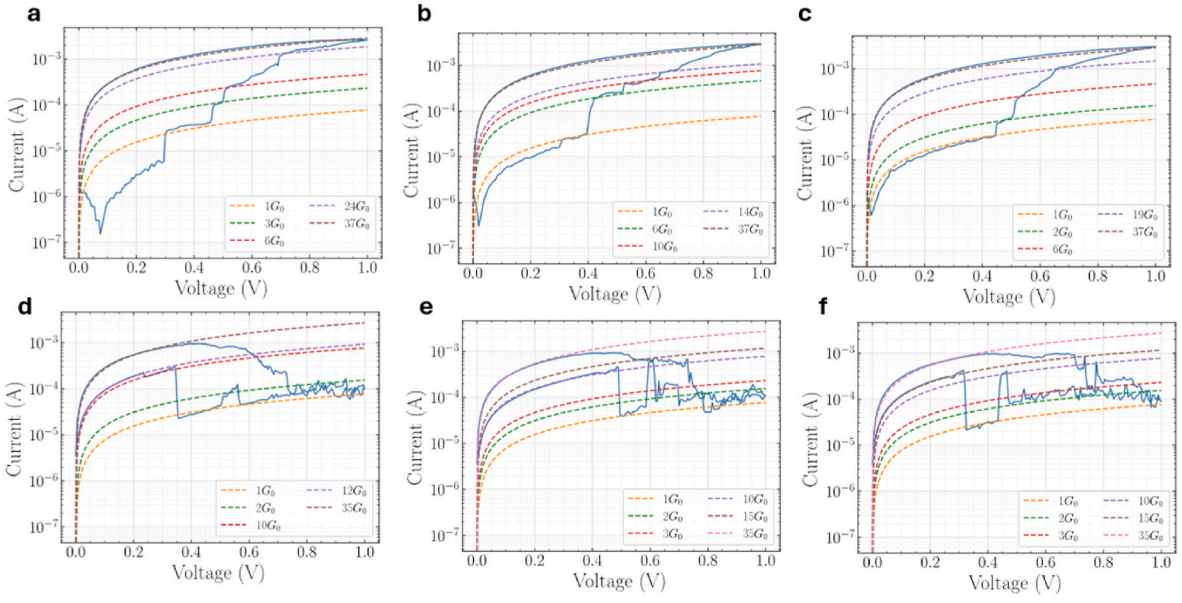


**Fig. 3.** **a (b, c)** Experimental set current versus voltage absolute value (solid blue lines), corresponding to cycles 35 (37, 61). Theoretical curves corresponding to $G_0$ multiples are shown for comparison in dashed lines. **d (e, f)** Experimental reset current versus voltage curves (solid blue lines), corresponding to cycles 27 (38, 94). Theoretical curves corresponding to $G_0$ multiples are shown for comparison in dashed lines. (For interpretation of the references to color in this figure legend, the reader is referred to the Web version of this article.)

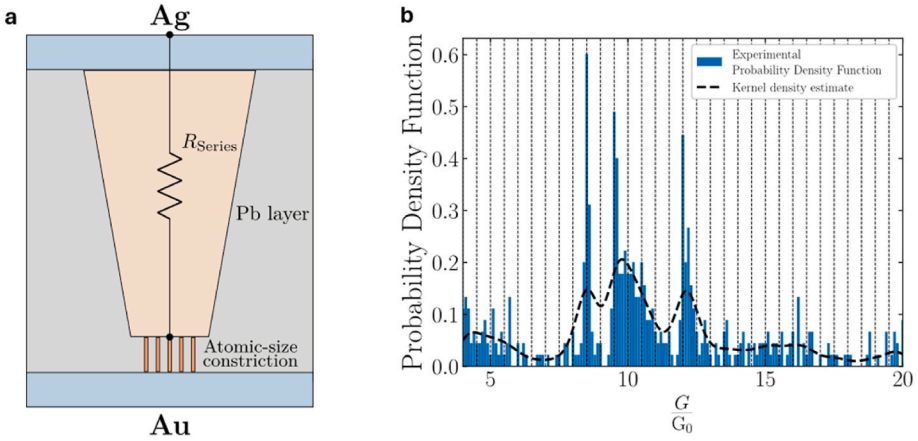


**Fig. 4.** **a** Scheme of the device with the components included in the current model proposed. **b** Experimental probability density function of the normalized conductance ($G/G_0$). A Gaussian kernel density estimation is shown in dashed lines.

$n_L$), assuming that the CF contains n single atomic constrictions, as depicted in Fig. 4a. It can also be seen as a wide constriction (equivalent to n atomic paths); they are equivalent, algebraically speaking. The inclusion of $R_{series}$ influences the voltage drop across the constrictions and, consequently, affects the total device conductance. In addition, as the switching process unfolds, the CF remnants change, producing a variation of its $R_{series}$. Therefore, its influence on measuring exact $G_0$ multiples or half-integer multiples changes every RS cycle (i.e., its influence in the denominator of Equation (2) varies).

In addition, Li et al. emphasize that in the quantum-point contact model, the voltage drop in each reservoir of the constriction can evolve with the actual filament geometry and its coupling with the reservoirs [46], also changing the device conductance. Other effects to take into consideration are impurities in the atomic-scale path or a non-adiabatic coupling with the reservoirs. In this context, the values of conductance below $G_0$ for each conductive mode are feasible [46]. Accordingly, a semiempirical approach could be used, in line with [92].

$$I \approx \frac{n\,\alpha\,G_0}{1 + n\,\alpha\,G_0 R_{series}} V \tag{3}$$

where parameter α incorporates all the non-idealities [92].

In the reset process depicted in Fig. 2c, there is a transition from

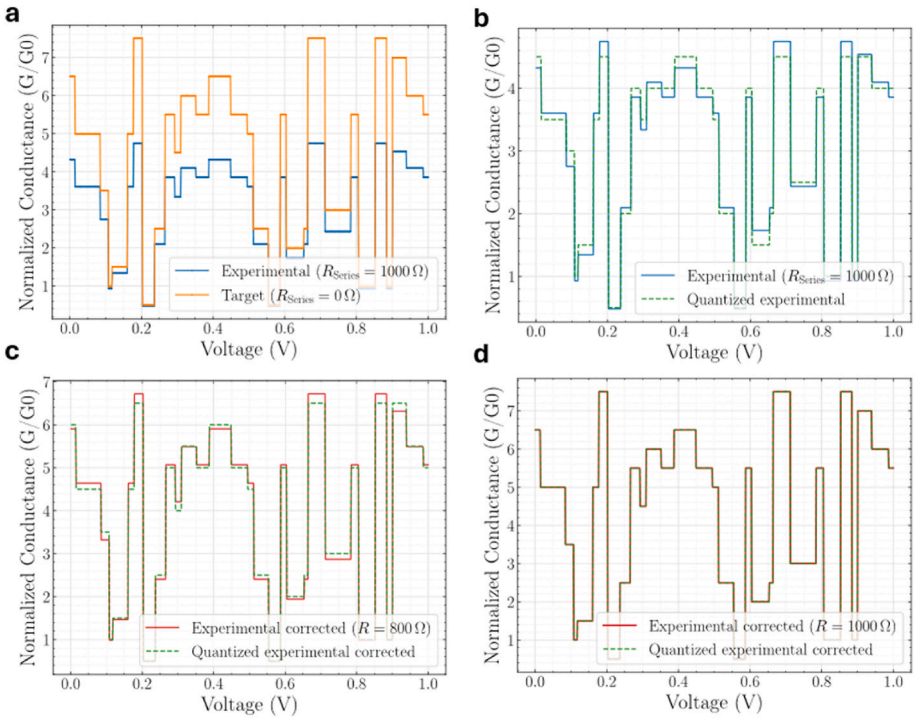


**Fig. 5.** **a** Normalized conductance versus voltage curve randomly generated by changing the number of atomic-size paths in a device ($R_{series}$ = 0Ω (1000Ω) and $\alpha$ = 0.5 for the orange (blue, the experimental curve) line) using Equation (3) (multiples and half-integers multiples of $G_0$ are allowed). **b** Normalized conductance curve (green line) generated with multiples and half-integer multiples of $G_0$ that minimizes the distance from the blue line. **c** Normalized conductance versus voltage curve of panel a (corresponding to blue in panel a) corrected back with $R_{series}$ = 800Ω (red) and quantized curve using multiples and half-integers multiples of $G_0$ (green). **d** Normalized conductance versus voltage curve of panel a (corresponding to blue in panel a) corrected back with $R_{series}$ = 1000Ω (red); i.e., the modification of panel a is corrected back and the quantized curve using multiples and half-integer multiples of $G_0$ (orange) perfectly matches the corrected curve, the mean square error between the two is minimized for $R_{series}$ = 1000Ω. In this case, the originally generated curve in panel a, in orange, is recovered. (For interpretation of the references to color in this figure legend, the reader is referred to the Web version of this article.)

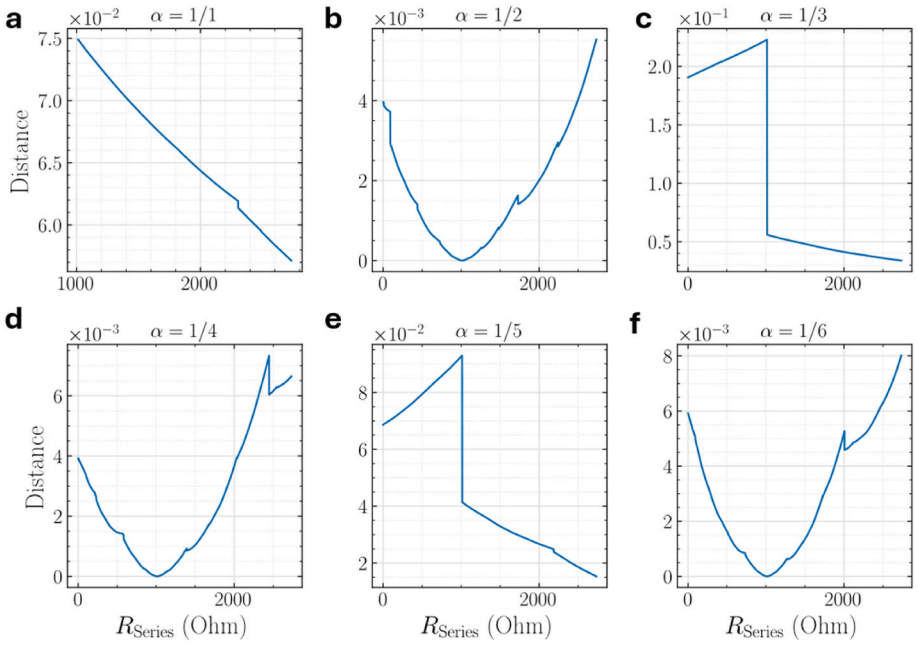


**Fig. 6. a (b, c, d, e, f)** Distance (or mean square error) between the generated curve of Fig. 5 (panel a, in orange) and those obtained correcting back with Equation (3) the blue curve in Fig. 5a for different series resistances and $\alpha$ (1/2, 1/3, 1/4, 1/5, 1/6). Notice that the series resistance has been swept for each of the alpha values employed in each panel searching for a zero distance, which is only found in some panels. (For interpretation of the references to color in this figure legend, the reader is referred to the Web version of this article.)

$10*G_0$ to $13*G_0$ at approximately 0.1V, then a current drop to $7*G_0$. The random nature of the physical mechanisms behind RS leads to these changes (even to a temporal current rise in a reset process). That can be modeled assuming the variation of the number of atomic constrictions in the dielectric. At 0.6V approximately, a sudden current drop of more than one order of magnitude suggests the rupture of most of the bundle of atomic constrictions that led the device to the LRS achieved in the previous set event.

In Fig. 3a, b, and 3c, different set I-V curves are plotted. The number of atomic constrictions (n in Equation (2)) rises as the set event progresses, lowering the device resistance toward the LRS. See that when the LRS is reached, the value of the current level is the same for all curves and corresponds to $37*G_0$, due to the compliance current limitation.

Fig. 4b shows the experimental normalized conductance ($G/G_0$) histogram obtained from the set I-V curves directly, without accounting for the series resistance. To improve the clarity of the results, we have fitted the experimental data within a kernel density estimation approach (several Gaussian distribution functions are employed to obtain the envelope that better fits the experimental data [93]). The fit allows to describe the peaks found at certain $G_0$ multiples that are particularly frequent, probably due to the CF or dielectric morphology that facilitates RS in these devices.

### 3.3. Discussion

We have employed the model described in Equation (3) to further analyze our data, assuming $0< \alpha \leq 1$. We have implemented a new algorithm to extract the series resistance in different steady-state I-V curves, such as those shown in Fig. 2a. To validate the procedure, prior to the use of experimental data, we generate an artificial dataset of normalized conductance versus voltage curve based on Equation (3) by randomly changing the number of atomic constrictions, assuming an arbitrary $R_{series} = 1000\Omega$ and $\alpha = 0.5$ (blue line in Fig. 5a, we call it "experimental curve"). This line represents the measured normalized conductance of a set of I-V curves. Then, we generate the same dataset (i.e., using the same number of atomic constrictions and alpha), but considering $R_{series} = 0\Omega$ (orange line in Fig. 5a). The goal of our algorithm is to calculate the series resistance.

We start from the experimental normalized conductance curve (blue line in Fig. 5a and b). It is assumed that conductance deviating from integer and half-integer values are due to the presence of a series resistance, which we aim to determine. To this end, a quantized version of the experimental conductance curve is constructed by assigning to each conductance value the nearest integer or half-integer value (green line in Fig. 5b). The distance (or minimum mean square error) between the experimental and the quantized curves indicates that the series resistance is non-zero.

The algorithm then subtracts (or corrects back) various resistance values from the experimental conductance curve in order to identify the resistance that minimizes the distance to its quantized counterpart (this is done by means of Equation (3)). If we subtract, for example, a resistance of 800Ω (see Fig. 5c), the distance between the new line and its quantized version decreases, indicating that we are adjusting the resistance correctly, although it is not correctly fitted. As shown in Fig. 5d, subtracting a series resistance of 1000Ω from the experimental curve yields a result that overlaps with its quantized version. This indicates that the series resistance of the device is 1000Ω, as we arbitrarily imposed for this test.

The procedure described in Fig. 5 suggests that $R_{series}$ could also be extracted from experimental data. Nevertheless, in this case, we do not have a first estimation of $R_{series}$. To solve this issue, we need to sweep the series resistance. In connection to $\alpha$ parameter, we neither have any "a priori" information. To illustrate how to proceed, we use again the data presented in Fig. 5. In Fig. 6, the mean square error (the distance metric) between the experimental normalized conductance curves and their quantized version for several series resistances and $\alpha$ values. The cases where the distance (or mean square error) is minimal (theoretically zero) correspond to the experimental series resistance. In this case, the minimum distance corresponds to a $R_{series} = 1000\Omega$, confirming the validity of our procedure.

It is observed that even values of the inverse of the alpha parameter behave alike, our procedure does not distinguish between them. This is because these values share the same quantization levels between them;

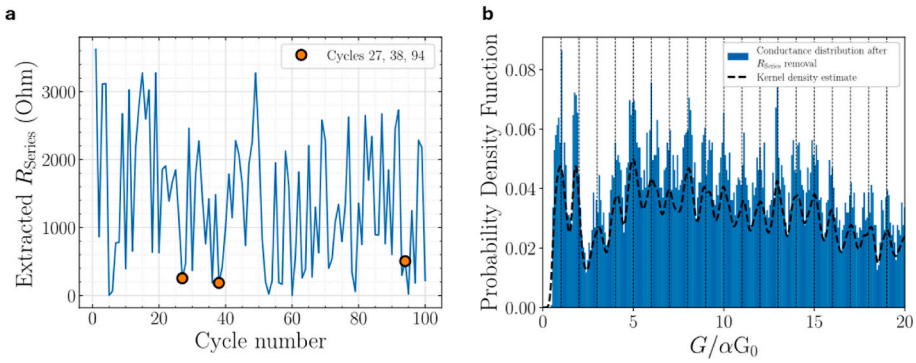


**Fig. 7.** **a** Extracted series resistance by using the proposed algorithm employing the experimental I-V curves measured for our PB devices. **b** Probability density function of the normalized (by $\alpha G_0$) experimental conductance values after correction by the series resistance. The kernel density estimations are shown in dashed lines.

e.g. if the curve is generated with $\frac{1}{\alpha} = 2$, then it will have conductances in 0.5 $G_0$, 1 $G_0$, 1.5 $G_0$, and so on, $\frac{1}{\alpha} = 4$ has conductance levels in 0.25 $G_0$, 0.5 $G_0$, 0.75 $G_0$, 1 $G_0$, etc. Because the same levels are shared, there is no difference in our algorithm when quantizing to $\frac{1}{\alpha} = 2$ and $\frac{1}{\alpha} = 4$, this happens for different integer multiples. In practice, because experimental alpha inverse is not likely to be an integer (we model using a continuous variable), it is rare to find two alphas with shared quantization levels. For this reason, we do not consider this coincidence an issue. The cases with odd $\frac{1}{\alpha}$ values do not show a minimum in the resistance range between zero and the maximum experimental resistance, so these values cannot be considered.

We can apply our technique to the experimental data shown in Fig. 2. The results are plotted in Fig. 7. We swept the series resistance, finding its optimal value, for each cycle and $\alpha$ parameter ($\alpha$ swept from 1/20 to 1), using the aforementioned extraction method. Then we extract the normalized conductances (dividing by $\alpha$ $G_0$) for each point in every cycle after the $\alpha$ and series resistance correction. Finally, we select the best $\alpha$ value as the one that minimizes the distance between the normalized conductances and the normalized quantized conductances.

We can observe cycles 27, 38, and 94, which we previously presented as examples of highly quantized curves (Fig. 3). These curves show a low series resistance with our procedure (orange circles in Fig. 7a), stating that quantization is directly distinguishable in the measured curve. We have corrected back the experimental curves for the series resistance and alpha parameter obtained in Fig. 7a. If we plot the corresponding probability density function, we see conductance peaks on all integer multiples of $\alpha G_0$, proving that our strategy increases the perceived quantization in the histogram. This indicates that the series resistance value is very low, according to Equation (3).

## 4. Conclusions

This work successfully presents the characterization and modeling of conductance quantization in RRAM devices utilizing PB-base as the dielectric material. Crucially, conductance quantization was observed, with current levels in both set and reset events corresponding to multiples of the quantum unit of conductance. Experimental data analysis revealed that certain $G_0$ multiples were particularly frequent, likely due to the CF configuration, which is linked to the dielectric morphology. This work not only verifies the phenomenon of conductance quantization in memristive devices utilizing PB but also provides critical advancements in modeling and characterization techniques. The developed algorithm for extracting series resistance and non-ideality parameters for the quantum conductance model significantly enhances the understanding of the underlying physical mechanisms in these devices. These findings underscore the potential of PB-based RRAMs for a wide range of future applications, including non-volatile memory circuits.

## CRediT authorship contribution statement

**A. Cantudo:** Writing – original draft, Visualization, Validation, Software, Investigation, Data curation, Conceptualization. **L.B. Avila:** Writing – review & editing, Resources, Investigation, Data curation. **M. A. Villena:** Writing – review & editing, Visualization, Investigation. **F. Jiménez-Molinos:** Writing – review & editing, Investigation. **C. Ducarme:** Investigation. **A. Lopes Temporao:** Investigation. **A. Moureaux:** Investigation. **F. Abreu Araujo:** Writing – review & editing, Investigation. **C.K. Müller:** Investigation, Writing -review & edit. **J.B. Roldán:** Writing – original draft, Visualization, Investigation, Writing -review & edit.

## Declaration of competing interest

The authors declare that they have no known competing financial interests or personal relationships that could have appeared to influence the work reported in this paper.

## Acknowledgements

Research supported by the project PID2022-139586NB-C44, funded by MCIN/AEI/10.13039/501100011033 and FEDER, EU; and supported by the Ramón y Cajal grant (RYC2022-035618-I), funded by MCIU/AEI/10.13039/501100011033, and by the FSE+. F.A.A. is a Research Fellow of the F.R.S.-FNRS. C.K.M. thanks the Deutsche Forschungsgemeinschaft for funding (No. 531524052).

## Supplementary data

Supplementary data to this article can be found online at https://doi.org/10.1016/j.mssp.2025.110253.

## Data availability

Data will be made available on request.

## References

[1] M. Lanza, et al., Memristive technologies for data storage, computation, encryption, and radio-frequency communication, Science 376 (6597) (June 2022), https://doi.org/10.1126/science.abj9979.
[2] D. Ielmini, R. Waser (Eds.), Resistive Switching, Wiley, Jan. 2016, https://doi.org/10.1002/9783527680870.
[3] M. Lanza, et al., The growing memristor industry, Nature 640 (8059) (Apr. 2025) 613–622, https://doi.org/10.1038/s41586-025-08733-5.
[4] Y.-C. Chiu, et al., A 40nm 2Mb ReRAM macro with 85% reduction in FORMING time and 99% reduction in page-write time using Auto-FORMING and auto-write

schemes. 2019 Symposium on VLSI Technology, IEEE, June 2019, pp. T232–T233, https://doi.org/10.23919/vlsit.2019.8776540.
[5] C.-C. Chou, et al., An N40 256K×44 embedded RRAM macro with SL-precharge SA and low-voltage current limiter to improve read and write performance. 2018 IEEE International Solid - State Circuits Conference - (ISSCC), IEEE, Feb. 2018, pp. 478–480, https://doi.org/10.1109/isscc.2018.8310392.
[6] C.-C. Chou, et al., A 22nm 96KX144 RRAM macro with a self-tracking reference and a low ripple charge pump to achieve a configurable read window and a wide operating voltage range. 2020 IEEE Symposium on VLSI Circuits, IEEE, June 2020, pp. 1–2, https://doi.org/10.1109/vlsicircuits18222.2020.9163014.
[7] C. Mead, M. Ismail (Eds.), Analog VLSI Implementation of Neural Systems, Springer US, 1989, https://doi.org/10.1007/978-1-4613-1639-8.
[8] F. Aguirre, et al., Hardware implementation of memristor-based artificial neural networks, Nat. Commun. 15 (1) (Mar. 2024), https://doi.org/10.1038/s41467-024-45670-9.
[9] F. Hui, et al., In situ observation of low-power nano-synaptic response in graphene oxide using conductive atomic force microscopy, Small 17 (26) (June 2021), https://doi.org/10.1002/smll.202101100.
[10] S.N. Danilin, S.A. Shchanikov, Neural network control over operation accuracy of memristor-based hardware. 2015 International Conference on Mechanical Engineering, Automation and Control Systems (MEACS), Dec. 2015, pp. 1–5, https://doi.org/10.1109/meacs.2015.7414916. IEEE.
[11] M.A. Mishchenko, et al., Inverted spike-rate-dependent plasticity due to charge traps in a metal-oxide memristive device, J. Phys. D Appl. Phys. 55 (39) (July 2022) 394002, https://doi.org/10.1088/1361-6463/ac79de.
[12] E. Pérez-Bosch Quesada, et al., Toward reliable compact modeling of multilevel 1T-1R RRAM devices for neuromorphic systems, Electronics 10 (6) (Mar. 2021) 645, https://doi.org/10.3390/electronics10060645.
[13] S. Yu, H. Jiang, S. Huang, X. Peng, A. Lu, Compute-in-Memory chips for deep learning: recent trends and prospects, IEEE Circ. Syst. Mag. 21 (3) (2021) 31–56, https://doi.org/10.1109/mcas.2021.3092533.
[14] A. Sebastian, M. Le Gallo, R. Khaddam-Aljameh, E. Eleftheriou, Memory devices and applications for in-memory computing, Nat. Nanotechnol. 15 (7) (Mar. 2020) 529–544, https://doi.org/10.1038/s41565-020-0655-z.
[15] M. Prezioso, F. Merrikh-Bayat, B.D. Hoskins, G.C. Adam, K.K. Likharev, D. B. Strukov, Training and operation of an integrated neuromorphic network based on metal-oxide memristors, Nature 521 (7550) (May 2015) 61–64, https://doi.org/10.1038/nature14441.
[16] K. Zhu, et al., Hybrid 2D/CMOS microchips for memristive applications, Nature 618 (2023) 57–62, https://doi.org/10.1038/s41586-023-05973-1.
[17] J. Tang, et al., Bridging biological and artificial neural networks with emerging neuromorphic devices: fundamentals, progress, and challenges, Adv. Mater. 31 (49) (Sept. 2019), https://doi.org/10.1002/adma.201902761.
[18] S. Yadav, et al., Ultralow powered 2D MoS2-Based memristive crossbar array for synaptic applications, ACS Appl. Mater. Interfaces 17 (18) (Apr. 2025) 26871–26880, https://doi.org/10.1021/acsami.5c00688.
[19] R. Romero-Zaliz, E. Pérez, F. Jiménez-Molinos, C. Wenger, J.B. Roldán, Influence of variability on the performance of HfO2 memristor-based convolutional neural networks, Solid State Electron. 185 (Nov. 2021) 108064, https://doi.org/10.1016/j.sse.2021.108064.
[20] C. Wang, et al., 2D layered materials for memristive and neuromorphic applications, Adv. Electron. Mater. 6 (2) (Dec. 2019), https://doi.org/10.1002/aelm.201901107.
[21] V. Milo, et al., Demonstration of hybrid CMOS/RRAM neural networks with spike time/rate-dependent plasticity. 2016 IEEE International Electron Devices Meeting (IEDM), Dec. 2016, pp. 16.8.1–16.8.4, https://doi.org/10.1109/iedm.2016.7838435. IEEE.
[22] A. Paul, et al., Scalable oxide-based memcapacitive crossbar arrays for 1 Kb neuromorphic memory, J. Phys. D Appl. Phys. 58 (23) (May 2025) 235103, https://doi.org/10.1088/1361-6463/add8a0.
[23] J.B. Roldan, et al., Spiking neural networks based on two-dimensional materials, npj 2D Mater Appl 6 (1) (2022) Sept, https://doi.org/10.1038/s41699-022-00341-5.
[24] Z. Wei, et al., True random number generator using current difference based on a fractional stochastic model in 40-nm embedded ReRAM. 2016 IEEE International Electron Devices Meeting (IEDM), IEEE, Dec. 2016, pp. 4.8.1–4.8.4, https://doi.org/10.1109/iedm.2016.7838349.
[25] B. Gao, et al., Concealable physically unclonable function chip with a memristor array, Sci. Adv. 8 (24) (June 2022), https://doi.org/10.1126/sciadv.abn7753.
[26] C. Wen, et al., Advanced data encryption using 2D materials, Adv. Mater. 33 (27) (May 2021), https://doi.org/10.1002/adma.202100185.
[27] H. Nili, et al., Hardware-intrinsic security primitives enabled by analogue state and nonlinear conductance variations in integrated memristors, Nat. Electron. 1 (3) (Mar. 2018) 197–202, https://doi.org/10.1038/s41928-018-0039-7.
[28] L. Chua, Memristor-the missing circuit element, IEEE Trans. Circ. Theor. 18 (5) (1971) 507–519, https://doi.org/10.1109/tct.1971.1083337.
[29] L.O. Chua, Sung Mo Kang, Memristive devices and systems, Proc. IEEE 64 (2) (1976) 209–223, https://doi.org/10.1109/proc.1976.10092.
[30] L. Chua, Resistance switching memories are memristors, Appl. Phys. A 102 (4) (Jan. 2011) 765–783, https://doi.org/10.1007/s00339-011-6264-9.
[31] S. Spiga, A. Sebastian, D. Querlioz, B. Rajendran, Role of resistive memory devices in brain-inspired computing. Memristive Devices for Brain-Inspired Computing, Elsevier, 2020, pp. 3–16, https://doi.org/10.1016/b978-0-08-102782-0.00001-0.
[32] D. Maldonado, et al., TiN/Ti/HfO2/TiN memristive devices for neuromorphic computing: from synaptic plasticity to stochastic resonance, Front. Neurosci. 17 (2023) Sept, https://doi.org/10.3389/fnins.2023.1271956.
[33] J. Reuben, D. Fey, C. Wenger, A modeling methodology for resistive RAM based on Stanford-PKU model with extended multilevel capability, IEEE Trans. Nanotechnol. 18 (2019) 647–656, https://doi.org/10.1109/tnano.2019.2922838.
[34] G. González-Cordero, et al., Analysis of resistive switching processes in TiN/Ti/HfO2/W devices to mimic electronic synapses in neuromorphic circuits, Solid State Electron. 157 (July 2019) 25–33, https://doi.org/10.1016/j.sse.2019.04.001.
[35] S. Poblador, M.B. Gonzalez, F. Campabadal, Investigation of the multilevel capability of TiN/Ti/HfO2/W resistive switching devices by sweep and pulse programming, Microelectron. Eng. 187 (188) (Feb. 2018) 148–153, https://doi.org/10.1016/j.mee.2017.11.007.
[36] G. Milano, et al., Quantum conductance in memristive devices: fundamentals, developments, and applications, Adv. Mater. 34 (32) (July 2022), https://doi.org/10.1002/adma.202201248.
[37] E. Miranda and J. Sune, "Analytic modeling of leakage current through multiple breakdown paths in SiO/sub 2/films," 2001 IEEE International Reliability Physics Symposium Proceedings. 39th Annual (Cat. No.00CH37167). IEEE, pp. 367–379. doi: 10.1109/relphy.2001.922929.
[38] E.A. Miranda, C. Walczyk, C. Wenger, T. Schroeder, Model for the resistive switching effect in HfO2 MIM structures based on the transmission properties of narrow constrictions, IEEE Electron Device Lett. 31 (6) (June 2010) 609–611, https://doi.org/10.1109/led.2010.2046310.
[39] D. Gall, Electron mean free path in elemental metals, J. Appl. Phys. 119 (8) (Feb. 2016), https://doi.org/10.1063/1.4942216.
[40] B.J. van Wees, et al., Quantized conductance of point contacts in a two-dimensional electron gas, Phys. Rev. Lett. 60 (9) (Feb. 1988) 848–850, https://doi.org/10.1103/physrevlett.60.848.
[41] H. Ohnishi, Y. Kondo, K. Takayanagi, Quantized conductance through individual rows of suspended gold atoms, Nature 395 (6704) (Oct. 1998) 780–783, https://doi.org/10.1038/27399.
[42] L. Chico, L.X. Benedict, S.G. Louie, M.L. Cohen, Quantum conductance of carbon nanotubes with defects, Phys. Rev. B 54 (4) (July 1996) 2600–2606, https://doi.org/10.1103/physrevb.54.2600.
[43] J. He, O. Sankey, M. Lee, N. Tao, X. Li, S. Lindsay, Measuring single molecule conductance with break junctions, Faraday Discuss. 131 (2006) 145–154, https://doi.org/10.1039/b508434m.
[44] J.B. Roldán, D. Maldonado, A. Cantudo, Y. Shen, W. Zheng, M. Lanza, Conductance quantization in h-BN memristors, Appl. Phys. Lett. 122 (20) (May 2023), https://doi.org/10.1063/5.0147403.
[45] A. Mehonic, et al., Quantum conductance in silicon oxide resistive memory devices, Sci. Rep. 3 (1) (2013) Sept, https://doi.org/10.1038/srep02708.
[46] Y. Li, et al., Conductance quantization in resistive random access memory, Nanoscale Res. Lett. 10 (1) (Oct. 2015), https://doi.org/10.1186/s11671-015-1118-6.
[47] Y. Lee, J. Park, D. Chung, K. Lee, S. Kim, Multi-level cells and quantized conductance characteristics of Al2O3-Based RRAM device for neuromorphic system, Nanoscale Res. Lett. 17 (1) (Sept. 2022), https://doi.org/10.1186/s11671-022-03722-3.
[48] L.B. Avila, et al., Resistive switching in electrodeposited prussian blue layers, Materials 13 (24) (Dec. 2020) 5618, https://doi.org/10.3390/ma13245618.
[49] F.L. Faita, et al., Abnormal resistive switching in electrodeposited Prussian white thin films, J. Alloys Compd. 896 (Mar. 2022) 162971, https://doi.org/10.1016/j.jallcom.2021.162971.
[50] L.B. Avila, P.C. Serrano Arambulo, A. Dantas, E.E. Cuevas-Arizaca, D. Kumar, C. K. Müller, Study on the electrical conduction mechanism of unipolar resistive switching prussian white thin films, Nanomaterials 12 (16) (Aug. 2022) 2881, https://doi.org/10.3390/nano12162881.
[51] L.B. Avila, et al., Prussian blue anchored on reduced graphene oxide substrate achieving high voltage in symmetric supercapacitor, Materials 17 (15) (Aug. 2024) 3782, https://doi.org/10.3390/ma17153782.
[52] Y. He, et al., Printed high-entropy prussian blue analogs for advanced non-volatile memristive devices, Adv. Mater. 37 (8) (Nov. 2024), https://doi.org/10.1002/adma.202410060.
[53] H.J. Buser, D. Schwarzenbach, W. Petter, A. Ludi, The crystal structure of Prussian blue: fe4[Fe(CN)6]3.xH2O, Inorg. Chem. 16 (11) (Nov. 1977) 2704–2710, https://doi.org/10.1021/ic50177a008.
[54] D.B. Brown, D.F. Shriver, Structures and solid-state reactions of Prussian blue analogs containing chromium, manganese, iron, and cobalt, Inorg. Chem. 8 (1) (Jan. 1969) 37–42, https://doi.org/10.1021/ic50071a009.
[55] D. Ito, S.-H. Jang, H. Ando, T. Momma, Y. Tateyama, Dissimilar diffusion mechanisms of Li+, Na+, and K+ ions in anhydrous Fe-Based prussian blue cathode, J. Am. Chem. Soc. 147 (29) (June 2025) 25441–25453, https://doi.org/10.1021/jacs.5c05274.
[56] S.-B. Hua, T. Jin, X. Guo, Electrochemical anodic oxidation assisted fabrication of memristors, Int. J. Extrem. Manuf. 6 (3) (Mar. 2024) 032008, https://doi.org/10.1088/2631-7990/ad2c61.
[57] L.B. Avila, et al., Variability analysis in memristors based on electrodeposited prussian blue, Microelectron. Eng. 300 (Nov. 2025) 112376, https://doi.org/10.1016/j.mee.2025.112376.
[58] J.B. Roldán, et al., Variability in resistive memories, Advanced Intelligent Systems 5 (6) (Mar. 2023), https://doi.org/10.1002/aisy.202200338.
[59] K. Terabe, T. Hasegawa, T. Nakayama, M. Aono, Quantized conductance atomic switch, Nature 433 (7021) (Jan. 2005) 47–50, https://doi.org/10.1038/nature03190.
[60] A. Geresdi, A. Halbritter, A. Gyenis, P. Makk, G. Mihály, From stochastic single atomic switch to nanoscale resistive memory device, Nanoscale 3 (4) (2011) 1504, https://doi.org/10.1039/c0nr00951b.

[61] S. Tappertzhofen, I. Valov, R. Waser, Quantum conductance and switching kinetics of AgI-based microcrossbar cells, Nanotechnology 23 (14) (Mar. 2012) 145703, https://doi.org/10.1088/0957-4484/23/14/145703.
[62] T. Tsuruoka, T. Hasegawa, K. Terabe, M. Aono, Conductance quantization and synaptic behavior in a Ta2O5-based atomic switch, Nanotechnology 23 (43) (Oct. 2012) 435705, https://doi.org/10.1088/0957-4484/23/43/435705.
[63] J.J.T. Wagenaar, M. Morales-Masis, J.M. van Ruitenbeek, Observing 'quantized' conductance steps in silver sulfide: two parallel resistive switching mechanisms, J. Appl. Phys. 111 (1) (Jan. 2012), https://doi.org/10.1063/1.3672824.
[64] J.R. Jameson, et al., Quantized conductance in Ag/$GeS_2$/W conductive-bridge memory cells, IEEE Electron Device Lett. 33 (2) (Feb. 2012) 257–259, https://doi.org/10.1109/led.2011.2177803.
[65] X.-J. Zhu, J. Shang, R.-W. Li, Resistive switching effects in oxide sandwiched structures, Front. Mater. Sci. 6 (3) (July 2012) 183–206, https://doi.org/10.1007/s11706-012-0170-8.
[66] X. Zhu, et al., Observation of conductance quantization in oxide-based resistive switching memory, Adv. Mater. 24 (29) (June 2012) 3941–3946, https://doi.org/10.1002/adma.201201506.
[67] E. Miranda, S. Kano, C. Dou, K. Kakushima, J. Suñé, H. Iwai, Nonlinear conductance quantization effects in CeOx/SiO2-based resistive switching devices, Appl. Phys. Lett. 101 (1) (July 2012), https://doi.org/10.1063/1.4733356.
[68] X. Lian, et al., Quantum point contact model of filamentary conduction in resistive switching memories. 2012 13th International Conference on Ultimate Integration on Silicon (ULIS), IEEE, Mar. 2012, pp. 101–104, https://doi.org/10.1109/ulis.2012.6193367.
[69] S. Gao, et al., Conductance quantization in a Ag filament-based polymer resistive memory, Nanotechnology 24 (33) (July 2013) 335201, https://doi.org/10.1088/0957-4484/24/33/335201.
[70] D. Liu, H. Cheng, X. Zhu, G. Wang, N. Wang, Analog memristors based on Thickening/Thinning of Ag nanofilaments in amorphous manganite thin films, ACS Appl. Mater. Interfaces 5 (21) (Oct. 2013) 11258–11264, https://doi.org/10.1021/am403497y.
[71] S. Long, et al., Quantum-size effects in hafnium-oxide resistive switching, Appl. Phys. Lett. 102 (18) (May 2013) 183505, https://doi.org/10.1063/1.4802265.
[72] C. Chen, et al., Conductance quantization in oxygen-anion-migration-based resistive switching memory devices, Appl. Phys. Lett. 103 (4) (July 2013), https://doi.org/10.1063/1.4816747.
[73] Y.-E. Syu, et al., Atomic-level quantized reaction of HfOx memristor, Appl. Phys. Lett. 102 (17) (Apr. 2013) 172903, https://doi.org/10.1063/1.4802821.
[74] C. Hu, M.D. McDaniel, J.G. Ekerdt, E.T. Yu, High ON/OFF ratio and quantized conductance in resistive switching of TiO2 on silicon, IEEE Electron Device Lett. 34 (11) (Nov. 2013) 1385–1387, https://doi.org/10.1109/led.2013.2282154.
[75] Y. Yang, et al., Electrochemical dynamics of nanoscale metallic inclusions in dielectrics, Nat. Commun. 5 (1) (June 2014), https://doi.org/10.1038/ncomms5232.
[76] S. Tappertzhofen, E. Linn, S. Menzel, A.J. Kenyon, R. Waser, I. Valov, Modeling of quantized conductance effects in electrochemical metallization cells, IEEE Trans. Nanotechnol. 14 (3) (May 2015) 505–512, https://doi.org/10.1109/tnano.2015.2411774.
[77] H. Lv, et al., Atomic view of filament growth in electrochemical memristive elements, Sci. Rep. 5 (1) (Aug. 2015), https://doi.org/10.1038/srep13311.
[78] V.K. Sahu, A.K. Das, R.S. Ajimsha, R. Singh, P. Misra, Tuneable quantised conductance memory states in TiO2 based resistive switching devices in crossbar geometry for high density memory applications, Nanotechnology 35 (29) (May 2024) 295203, https://doi.org/10.1088/1361-6528/ad403c.
[79] L. Jiang, et al., Conductance quantization in an AgInSbTe-based memristor at nanosecond scale, Appl. Phys. Lett. 109 (15) (Oct. 2016), https://doi.org/10.1063/1.4963263.
[80] J. Ge, M. Chaker, Oxygen vacancies control transition of resistive switching mode in single-crystal TiO2 memory device, ACS Appl. Mater. Interfaces 9 (19) (May 2017) 16327–16334, https://doi.org/10.1021/acsami.7b03527.
[81] S. Deswal, A. Kumar, A. Kumar, Investigating unipolar switching in Niobium oxide resistive switches: correlating quantized conductance and mechanism, AIP Adv. 8 (8) (Aug. 2018), https://doi.org/10.1063/1.5040466.
[82] Q. Chen, et al., Controlled construction of atomic point contact with 16 quantized conductance states in oxide resistive switching memory, ACS Appl. Electron. Mater. 1 (5) (Apr. 2019) 789–798, https://doi.org/10.1021/acsaelm.9b00191.
[83] Z. Xie, et al., Magnetism modulation and conductance quantization in a gadolinium oxide memristor, Phys. Chem. Chem. Phys. 22 (45) (2020) 26322–26329, https://doi.org/10.1039/d0cp03767b.
[84] M.H. Peng, et al., Dynamic behaviors and training effects in TiN/Ti/HfOx/TiN-nanolayered memristors with controllable quantized conductance states: implications for quantum and neuromorphic computing devices, ACS Appl. Nano Mater. 4 (2021) 11296, https://doi.org/10.1021/acsanm.1c02969.
[85] R.D. Nikam, K.G. Rajput, H. Hwang, Single-atom quantum-point contact switch using atomically thin hexagonal boron nitride, Small 17 (7) (Jan. 2021), https://doi.org/10.1002/smll.202006760.
[86] Y. Nishi, Improvement of appearance probability of conductance quantization by hydrogen thermal treatment in Pt/NiO/Pt-resistive switching cells, MRS Advances 6 (22) (Aug. 2021) 554–557, https://doi.org/10.1557/s43580-021-00127-9.
[87] O.G. Kharlanov, B.S. Shvetsov, V.V. Rylkov, A.A. Minnekhanov, Stability of quantized conductance levels in memristors with copper filaments: toward understanding the mechanisms of resistive switching, Phys. Rev. Appl. 17 (5) (May 2022), https://doi.org/10.1103/physrevapplied.17.054035.
[88] K. Hadiyal, R. Ganesan, R. Thamankar, Quantized conductance and multilevel memory operation in Mn3O4 nanowire network devices combined with low voltage operation and oxygen vacancy induced resistive switching, Adv. Electron. Mater. 11 (14) (July 2025), https://doi.org/10.1002/aelm.202500159.
[89] C. Pan, et al., Model for multi-filamentary conduction in graphene/hexagonal-boron-nitride/graphene based resistive switching devices, 2D Mater. 4 (2) (May 2017) 025099, https://doi.org/10.1088/2053-1583/aa7129.
[90] D. Maldonado, et al., Experimental study of the series resistance effect and its impact on the compact modeling of the conduction characteristics of $HfO_2$-based resistive switching memories, J. Appl. Phys. 130 (5) (Aug. 2021), https://doi.org/10.1063/5.0055982.
[91] C. Walczyk, et al., Impact of temperature on the resistive switching behavior of embedded HfO2-Based RRAM devices, IEEE Trans. Electron. Dev. 58 (9) (Sept. 2011) 3124–3131, https://doi.org/10.1109/ted.2011.2160265.
[92] J. Suñé, F. Aguirre, M. Bargalló González, F. Campabadal, E. Miranda, Exploring conductance quantization effects in electroformed filaments for their potential application to a resistance standard, Adv. Quantum Technol. 6 (7) (May 2023), https://doi.org/10.1002/qute.202300048.
[93] W. Härdle, A. Werwatz, M. Müller, S. Sperlich, Nonparametric and Semiparametric Models, Springer Berlin Heidelberg, 2004, https://doi.org/10.1007/978-3-642-17146-8.